

Check for updates







Fluorinated Rocksalt-Polyanion Cathode for Lithium-Ion **Batteries**

Yimeng Huang¹ | Yaoshen Niu² | Zhen Zhang² | Zihan Lin² | Weiyin Chen¹ | Vivienne Yiwei Liu² | Iradwikanari Waluyo³ | Adrian Hunt³ | Xianghui Xiao³ | Yanhao Dong⁴ D | Ju Li^{1,2}

¹Department of Nuclear Science and Engineering, Massachusetts Institute of Technology, Cambridge, Massachusetts, USA | ²Department of Materials Science and Engineering, Massachusetts Institute of Technology, Cambridge, Massachusetts, USA | 3National Synchrotron Light Source II, Brookhaven National Laboratory, Upton, New York, USA | 4State Key Laboratory of New Ceramic Materials, School of Materials Science and Engineering, Tsinghua University, Beijing, China

Correspondence: Yanhao Dong (dongyanhao@tsinghua.edu.cn) | Ju Li (liju@mit.edu)

Received: 3 July 2025 | Revised: 31 August 2025 | Accepted: 9 September 2025

ABSTRACT

Integrated rocksalt-polyanion cathodes (DRXPS) are promising candidates for next-generation lithium-ion battery cathode materials that combine high energy density, stable cycling performance, and reduced reliance on Co and Ni. In this work, we investigated Li₃Mn₁₆P_{0.4}O_{5.4}F_{0.6}, a new DRXPS cathode with fluoride incorporation. A pure spinel phase was formed and a discharge capacity retention of 84% was achieved after 200 cycles between 1.5 and 4.8 V versus Li/Li⁺. In comparison, the similarly synthesized Li₃Mn_{1.6}Nb_{0.4}O_{5.4}F_{0.6}, in which all P⁵⁺ was substituted by Nb⁵⁺ while maintaining the same stoichiometry for all other elements, crystallized in a disordered rocksalt structure, and exhibited inferior capacity retention and rate capability than the P^{5+} counterpart. Our findings expand the compositional space of DRXPS to include F⁻, justify the viability of integrating polyanion groups in rocksalt-type cathodes, and highlight the superiority of P⁵⁺ as a cation charge compensator compared to the commonly used Nb⁵⁺. This work thereby advances the design of robust, high-performance cathode materials for sustainable batteries.

Introduction

The continuous growth in global energy demand and the critical need for sustainable and affordable battery technologies have intensified research efforts toward next-generation lithium-ion batteries (LIBs). Conventional layered cathode materials that rely heavily on Co and Ni face significant limitations due to resource scarcity, ethical sourcing issues, and price volatility [1, 2]. There is a great urgency in developing alternative earth-abundant, Co- and Ni-free cathode materials with high energy density and stable cycling performance.

Disordered rocksalt (DRX) cathodes have emerged as attractive alternatives, offering high theoretical capacities, elemental abundance, and compositional flexibility, thereby presenting significant promise for sustainable battery technologies [3-7]. Nevertheless, DRX cathodes often exhibit limited cycling stability owing to structural instabilities, volume expansion, and oxygen loss during electrochemical cycling [5, 8]. To overcome these issues, integrated rocksalt-polyanion cathodes (DRXPS) [9] have recently been introduced to address these stability challenges. By incorporating small amounts of polyanion groups (PO₄³⁻, BO₃³⁻, SiO₄⁴⁻, etc.) that have strong covalent bonds with oxygen atoms into a cation-deficient rocksalt framework, much-improved cycling performance can be achieved without compromising the overall energy density, making this approach particularly promising. Interestingly, the addition of polyanion groups also modifies the cation ordering within the face-centered cubic (FCC) oxygen framework, shifting from a rocksalt structure in DRX to a spinel structure in DRXPS. Since (partially) disordered rocksalt structures are not constrained to layered arrangements and possess substantial free volume created by Li excess and cation deficiency, DRX and DRXPS cathodes offer an extensive compositional space that are largely unexplored [5, 8, 9], and the concept of polyanion integration for better stability awaits further validation.

This is an open access article under the terms of the Creative Commons Attribution License, which permits use, distribution and reproduction in any medium, provided the original work is properly

© 2025 The Author(s). Interdisciplinary Materials published by Wuhan University of Technology and John Wiley & Sons Australia, Ltd.

In this study, we investigated a fluorine-containing DRXPS composition Li₃Mn_{1.6}P_{0.4}O_{5.4}F_{0.6} (DRXPS-P-F), in which P⁵⁺ is incorporated into a cation-deficient rocksalt structure and F partially substitutes O²⁻ (Figure 1). Fluorine doping in DRX materials is known to lower transition metal oxidation states, enhance lithium-ion mobility, and improve electrochemical performance by altering short-range order or reducing the material's impedance and enhancing diffusion pathways [10-13]. Here, we demonstrate that Li₃Mn_{1.6}P_{0.4}O_{5.4}F_{0.6} forms a spinel-type phase, and exhibits good rate performance and cycling stability (84% capacity retention after 200 cycles). In addition to stabilizing oxygen, phosphorus with +5 oxidation state also serves as a cationic charge compensator for lowering the as-synthesized Mn valence and thus increasing cationic redox contribution to capacity. To assess the effectiveness of P5+, we similarly synthesized and tested a comparative material, Li₃Mn_{1.6}Nb_{0.4}O_{5.4}F_{0.6} (DRX-Nb-F), replacing P⁵⁺ with Nb⁵⁺, a widely used high-valent cationic charge compensator in DRX cathodes [4, 5, 8] (Figure 1). It has the same starting Mn valence as DRXPS-P-F. Li $_3$ Mn $_{1.6}$ Nb $_{0.4}$ O $_{5.4}$ F $_{0.6}$ crystallizes in a disordered rocksalt structure without spinel order, and exhibits inferior electrochemical performance than the P $^{5+}$ counterpart (capacity retention of 58% after 150 cycles, larger polarization, and higher gas evolution). These findings highlight P $^{5+}$ as a superior choice to Nb $^{5+}$ for cationic charge compensation in rocksalt cathodes, and demonstrate good compatibility between P $^{5+}$ and F $^-$, the anionic charge compensator. The expanded compositional space of DRXPS cathodes and the superior cycling stability of the fluorinated DRXPS demonstrated in this work underscore great potential of DRXPS cathodes for next-generation sustainable batteries.

2 | Results and Discussion

2.1 | Structural Properties

DRXPS-P-F and DRX-Nb-F were synthesized using a low-temperature mechanochemical method, since the high-temperature

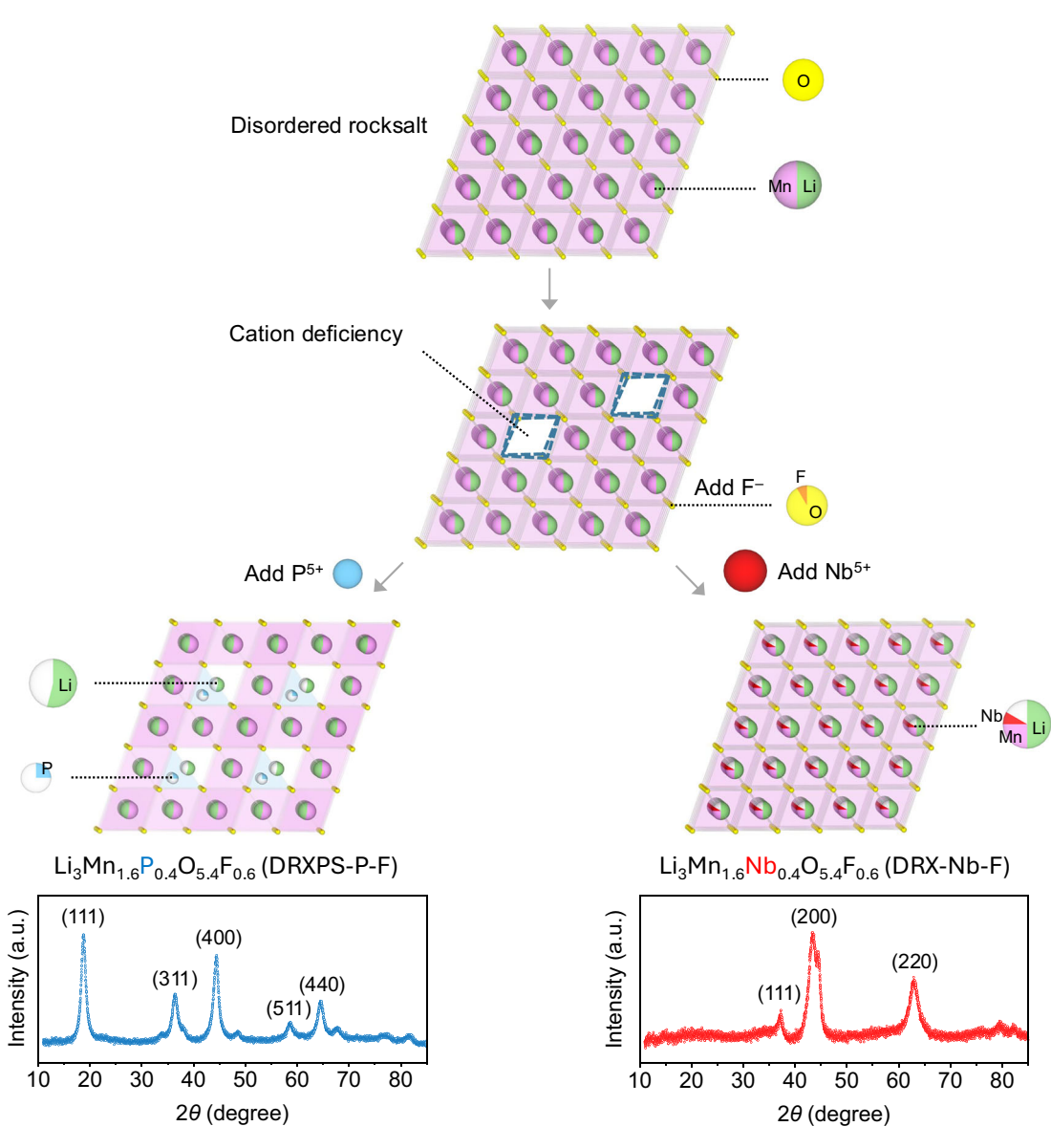


FIGURE 1 | Design of fluorinated rocksalt cathodes. P^{5+} and Nb^{5+} are incorporated into a cation-deficient DRX LiMnO₂ structure with F^- partially substituting O^{2-} . XRD patterns of DRXPS-P-F (bottom-left) and DRX-Nb-F (bottom-right).

2 Interdisciplinary Materials, 2025

solid solubility of F is very low [5, 14]. Their exact compositions are close to the intended targets of $\text{Li}_3\text{Mn}_{1.6}\text{P}_{0.4}\text{O}_{5.4}\text{F}_{0.6}$ (DRXPS-P-F) and Li₃Mn_{1.6}Nb_{0.4}O_{5.4}F_{0.6} (DRX-Nb-F) respectively, as confirmed by inductively coupled plasma optical emission spectrometry (ICP-OES) (Supporting Information S1: Table S1). XRD patterns show that DRXPS-P-F has a single-phase spinel-like cubic structure (Figure 1, bottom left) ($\alpha = \beta = \gamma = 90^{\circ}$). Rietveld refinement (Supporting Information S1: Figure S1A and Supporting Information S1: Table S2) yields lattice parameters a = b = c = 8.1689 Å. The main peaks at 19°, 36°, 44°, 59°, and 65° correspond to the (111), (311), (400), (511), and (440) planes of a cubic spinel structure, respectively. DRXPS-P-F has slightly smaller lattice parameters than the reference spinel LiMn₂O₄ (a = b = c = 8.2445 Åand $\alpha = \beta = \gamma = 90^{\circ}$) (Supporting Information S1: Figure S1B), but otherwise the two XRD patterns match well. In comparison, DRX-Nb-F has a disordered rocksalt-like structure (Figure 1, bottom right), with main peaks at 37°, 44° and 63° that correspond to the (111), (200), and (220) planes, respectively (the small split peak at 44° is likely due to splitting). Rietveld refinement (Supporting Information S1: Figure S2 and Supporting Information S1: Table S3) yields lattice parameters $a = 4.1530 \,\text{Å}$. The XRD results suggest that P⁵⁺ promotes the formation of a spinel-like order, while Nb⁵⁺ favors a disordered rocksalt structure. This is consistent with the fact that P⁵⁺ with small ionic radius prefers tetrahedral coordination that is commonly found in spinel-like frameworks [15, 16], while the octahedrally-coordinated Nb5+ is a d0 ion that is beneficial for stabilizing disordered rocksalt structures, since it can easily displace from its octahedron center at a low energy cost [5, 8, 17].

For more insights on the local structure, Raman spectroscopy measurements were conducted on DRXPS-P-F (Supporting Information S1: Figure S3) and DRX-Nb-F (Supporting Information S1: Figure S4). For DRXPS-P-F, the double peaks at 420-490 cm⁻¹ correspond to the symmetric stretching mode of LiO_4 [18] and LiO_6 [18], the peak around 600 cm⁻¹ corresponds to the symmetric stretching mode of MnO₆ [18, 19], and the peak around 950 cm⁻¹ corresponds to the A_{1g} mode of PO₄ [20]. These Raman features indicate octahedral occupation of Mn, tetrahedral occupation of P, and hybrid tetrahedral and octahedral occupations of Li for DRXPS-P-F. For DRX-Nb-F, the peak around 480 cm⁻¹ with minimal splitting likely corresponds to the symmetric stretching mode of LiO₆, suggesting that Li adopts one type of structural configuration. The peak around 600 cm⁻¹ corresponds to the symmetric stretching mode of MnO₆ [18, 19], and the peak around 870 cm⁻¹ corresponds to the antisymmetric stretching mode of NbO₆ [21, 22]. These Raman features indicate octahedral occupation of Li, Mn, and Nb for DRX-Nb-F.

With the XRD and Raman measurement results above, a structural model for DRXPS-P-F was proposed (Figure 1, bottom left), which is a cubic spinel structure that consists of a close-packed anion sublattice at 32e site occupied by O (90%) and F (10%), 16 d octahedral site for cations occupied by Mn (53.3%, by placing all Mn at this site) and Li (46.7%, by assuming full occupation at 16 d site without vacancy), and 8a tetrahedral site for cations occupied by P (6.7%, by placing all P at this site). The remaining Li should occupy 8a tetrahedral site and 16c octahedral site. The structural information can be summarized as $(P_{0.4}\text{Li}_x\Box_{5.6-x})_{\text{Tet-8a}}(\text{Li}_{1.6-x}\Box_{1.4})_{\text{Oct-16c}}(\text{Li}_{1.4}\text{Mn}_{1.6})_{\text{Oct-16d}}(O_{5.4}F_{0.6})_{32e}$, where $0 \le x \le 1.6$, \Box denotes vacancy (unoccupied site), Tet denotes tetrahedral sites, and Oct denotes

octahedral sites. The 16d and 32e sites make up the spinel framework. A structural model was also proposed for DRX-Nb-F (Figure 1, bottom right), where Li/Mn/Nb occupy octahedral 4a sites, and O/F occupy 4b sites. The structural information can be summarized as $(\text{Li}_3\text{Mn}_{1.6}\text{Nb}_{0.4}\square)_{\text{Oct-4a}}(O_{5.4}F_{0.6})_{4b}$.

For morphological information, scanning electron microscopy (SEM) was performed on DRXPS-P-F (Figure 2A) and DRX-Nb-F (Figure 2D). Both samples have particle sizes of around 100-300 nm and have minor agglomerations. These are typical microstructures in mechanochemically synthesized DRX cathodes [4, 6, 9, 23]. For elemental distributions, energydispersive spectrometry (EDS) mapping was conducted on DRXPS-P-F (Figure 2B) and DRX-Nb-F (Figure 2E). Both samples show uniform Li, Mn, P/Nb, O, and F distributions in the as-synthesized state. Transmission electron microscopy (TEM) images and selected area electron diffraction (SAED) patterns (Figure 2C,F) show that the particles of DRXPS-P-F and DRX-Nb-F are polycrystalline in nature, while the true "primary particle size" should be in the sub-10 nm regime. Characteristic lattice spacing of 4.7 Å and 2.4 Å were measured for DRXPS-P-F (inset of Figure 2C, corresponding to (111) planes) and DRX-Nb-F (inset of Figure 2F, corresponding to (111) planes), respectively. They are also consistent with the XRD data and support the crystallinity of the samples, albeit nano-grain sizes.

2.2 | Electrochemical Performance With Stabilized Cycling

The electrochemical properties of DRXPS-P-F and DRX-Nb-F were evaluated in coin-type half cells, cycled between 1.5 and 4.8 V vs Li/Li⁺ at room temperature (25°C). Figure 3A shows their first-cycle voltage profiles at 20 mA g⁻¹. Discharge capacities of 266 and 285 mAh g⁻¹ and discharge energy densities of 819 and 869 Wh kg⁻¹ were achieved for DRXPS-P-F and DRX-Nb-F, respectively. In the first discharge, DRXPS-P-F shows voltage plateaus at ~4 V and ~3 V, similar to ones in over-discharged spinel LiMn₂O₄, which correspond to tetrahedral and octahedral Li insertion, respectively [1, 24]. In comparison, DRX-Nb-F has a sloping voltage profile without any obvious voltage plateaus. This is a typical observation for DRX cathodes and may indicate massive structural relaxations/re-organizations accompanied by high-voltage charging and active oxygen redox [5].

The rate performance of DRXPS-P-F and DRX-Nb-F was evaluated from 20 to $1000\,\mathrm{mA}\,\mathrm{g}^{-1}$. As shown in Figure 3B, DRXPS-P-F has better rate performance than DRX-Nb-F, with 44% capacity retention at $1000\,\mathrm{mA}\,\mathrm{g}^{-1}$ compared to that at $20\,\mathrm{mA}\,\mathrm{g}^{-1}$, while DRX-Nb-F has only 25% retention. Galvano-static intermittent titration technique (GITT) measurements were conducted on DRXPS-P-F and DRX-Nb-F in the 2nd cycle to further reveal their diffusion kinetics (Figure 3C,D). From GITT profiles, much smaller nonohmic overpotentials were observed for DRXPS-P-F compared to DRX-Nb-F (Supporting Information S1: Figure S5) during both charge and discharge. This indicates that DRXPS-P-F has better Li⁺ diffusion kinetics than DRX-Nb-F, which likely benefitted from the three-dimensional Li⁺ diffusion pathways offered by the spinel structure [15, 23] (note that the Ohmic losses are similar for both materials due to the similar

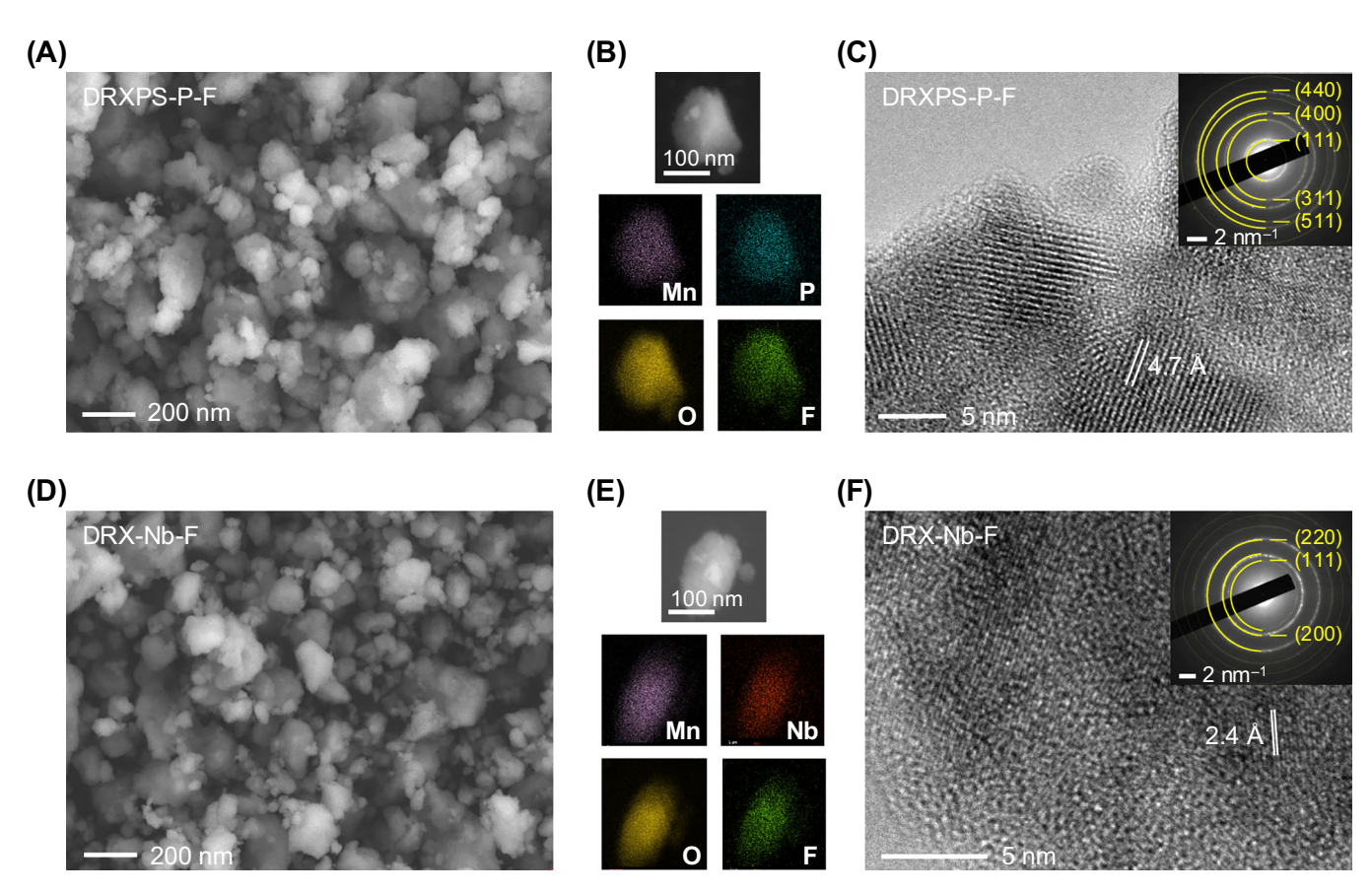


FIGURE 2 | Morphological characterizations. (A) SEM image, (B) STEM-EDS mapping and (C) HRTEM image of DRXPS-P-F. Inset: selected area electron diffraction pattern. (D) SEM image, (E) STEM-EDS mapping, and (F) HRTEM image of DRX-Nb-F. Inset: selected area electron diffraction pattern.

electrode architecture). This is consistent with diffusivity calculations (Figure 3E,F), which show almost tenfold increase in the average Li⁺ diffusivity for DRXPS-P-F over DRX-Nb-F in both charge $(1.75\times10^{-10}~{\rm vs.}~2.06\times10^{-11}~{\rm cm^2~s^{-1}})$ and discharge $(1.76\times10^{-10}~{\rm vs.}~1.91\times10^{-11}~{\rm cm^2~s^{-1}})$.

Cycling performance for DRXPS-P-F and DRX-Nb-F was tested between 1.5 and 4.8 V versus Li/Li^+ at 50 mA g^{-1} (~0.25 C), following three formation cycles at 20 mA g^{-1} . Shown in Figure 4A, DRXPS-P-F has a capacity retention of 84% and a voltage retention of 98% after 200 cycles (with respect to the first cycle at 50 mA g⁻¹; formation cycles were not shown). These are much better than the capacity retention of 52% and voltage retention of 84% for DRX-Nb-F. The superior cycling stability of DRXPS-P-F is further illustrated by the charge-discharge curves at the 5th, 25th, 100th, and 200th cycles at 50 mA g⁻¹ (Figure 4B), which show stable voltage profiles and small capacity/voltage decays over extended cycles. In comparison, DRX-Nb-F shows much faster decays in both capacity and average voltage. This further validates the key design concept of DRXPS cathodes, which is improving the cycling stability of high-voltage oxide cathodes (with an upper cutoff voltage of > 4.5 V vs Li/Li⁺) by polyanion incorporation, where the strong X-O covalent bond in polyanions (X = P in this case) stabilizes labile oxygen and reduces oxygen evolution at high voltages [9, 25, 26]. To quantify the outgassing of oxidized oxygen species, differential electrochemical mass spectrometry (DEMS) measurements were performed. As shown in Supporting Information S1: Figure S6, DRXPS-P-F shows less gas evolution (CO_2 and O_2) than DRX-Nb-F in the first cycle, providing evidence for the stabilized oxygen.

2.3 | Redox Mechanism

To study the redox mechanism, ex situ Raman spectroscopy, X-ray absorption near-edge structure (XANES) measurement on the Mn K-edge, soft X-ray absorption spectroscopy (sXAS) on the Mn L-edge (under PFY mode i.e. sensitive to the bulk chemistry), and high-resolution X-ray photoelectron spectroscopy (HR-XPS) were performed on DRXPS-P-F electrodes under different states of charge (Figure 5A, including pristine state, and 4.8 V-charged, 3.5 V-discharged, 2.5 V-discharged, and 1.5 V-discharged states in the first cycle). From the Raman spectra in Figure 5B, it is clear that minimal changes take place on the peak at around 940 cm⁻¹ (corresponding to PO₄), while the peak at around 600 cm⁻¹ (corresponding to MnO₆) shifts under different states of charge. From the Raman shifts of the peak positions (Figure 5B inset), a clear monotonic dependence is observed for the MnO6 peak on the degree of lithiation in DRXPS-P-F, which is an indication of the changes in Mn valence and the Mn-O bond length (lower Mn valence and thus longer Mn-O bond length cause negative Raman shifts). On the other hand, the minimal shifts of the PO₄ peak indicate that PO₄ polyanions have strong structural integrity that is beneficial for the overall structural stability of the material. This can also

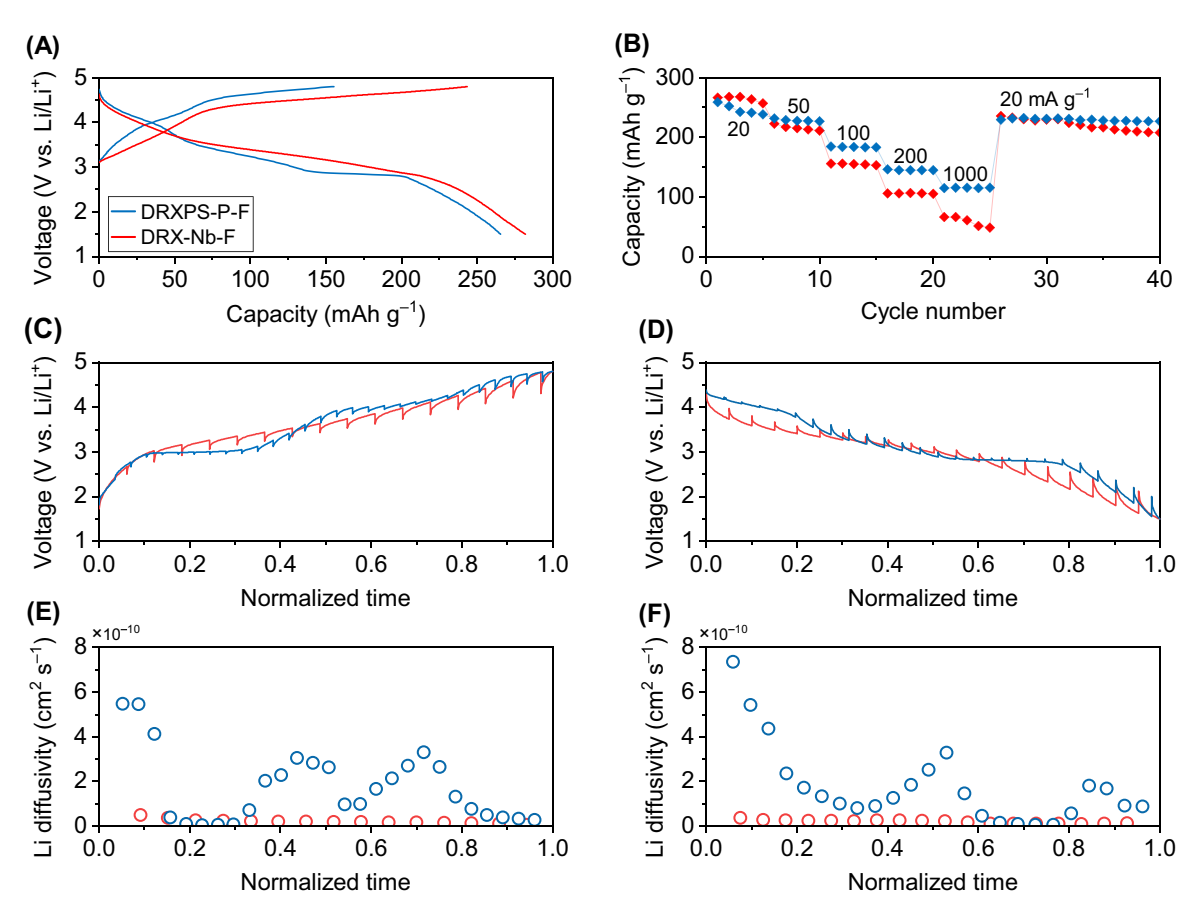


FIGURE 3 | Voltage profile and rate capability. (A) Voltage profiles of DRXPS-P-F and DRX-Nb-F in the first cycle, cycled between 1.5 and 4.8 V versus Li/Li⁺ at 20 mA g⁻¹. (B) Rate performance of DRXPS-P-F and DRX-Nb-F, cycled between 1.5 and 4.8 V versus Li/Li⁺ at 20, 50, 200, 500 and 1000 mA g⁻¹. GITT profiles of DRXPS-P-F and DRX-Nb-F in the (C) 2nd charge and (D) 2nd discharge cycle. Li diffusivity of DRXPS-P-F and DRX-Nb-F at each GITT step during the (E) 2nd charge and (F) 2nd discharge cycle.

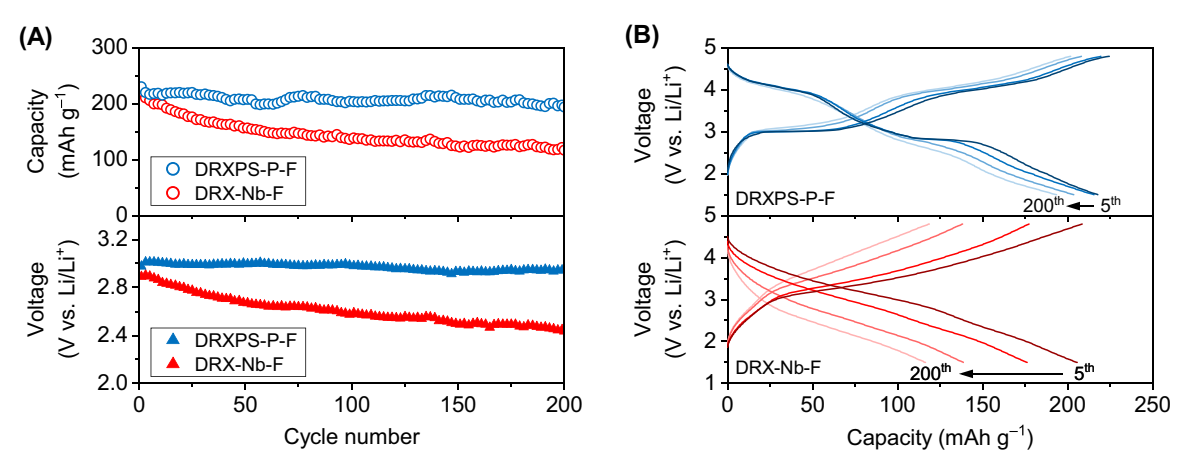


FIGURE 4 | Cycling stability and gas evolution. (A) Capacity (top) and voltage (bottom) retention of DRXPS-P-F and DRX-Nb-F, cycled between 1.5 and 4.8 V vs Li/Li^+ at 50 mA g^{-1} . (B) Voltage profiles of DRXPS-P-F (top) and DRX-Nb-F (bottom) at the 5th, 25th, 100th, and 200th cycle, cycled between 1.5 and 4.8 V versus Li/Li^+ at 50 mA g^{-1} .

be confirmed by HR-XPS that shows P remains in the +5 oxidation state at the charged state after more than 200 cycles (Supporting Information S1: Figure S7B,C), and by *ex situ* XRD that shows the spinel ordering is retained during charge/discharge for DRXPS-P-F (Supporting Information S1: Figure S8). In addition, better thermal stability is observed for DRXPS-P-F, which exhibits a higher onset temperature of rapid weight loss

than DRX-Nb-F, as shown in the thermogravimetric analysis (TGA) results (Supporting Information S1: Figure S9).

More direct evidence of Mn redox activity in DRXPS-P-F was obtained by synchrotron hard and soft X-ray absorption spectroscopy. Mn K-edge XANES measurement using hard X-rays, shown in Figure 5C, reveals that the pristine, 4.8

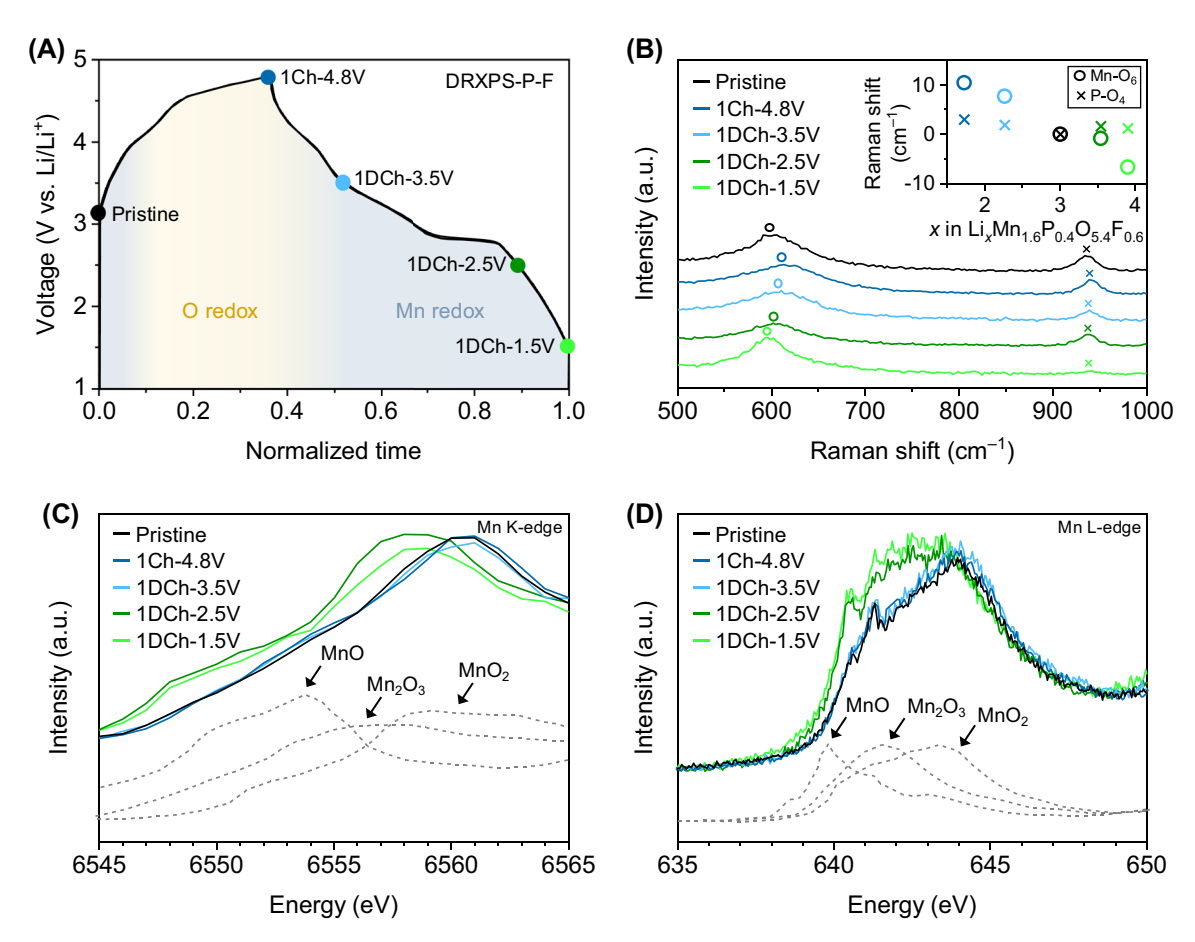


FIGURE 5 | Structural change and redox mechanism of DRXPS-P-F. (A) First cycle voltage profile of DRXPS-P-F, cycled between 1.5 and 4.8 V versus Li/Li⁺ at 20 mA g⁻¹. Colored points indicate voltages at which *ex situ* electrode samples are taken for X-ray absorption and Raman measurements. Regions dominated by O and Mn redox are shown as orange and blue colors under the curve, respectively. (B) *Ex situ* Raman spectra of DRXPS-P-F between 500 and 1000 cm⁻¹. Inset: Mn-O₆ (left) and P-O₄ (right) Raman peak shift relative to pristine sample under different states of charge. (C) *Ex situ* XANES measurement of Mn K-edge of DRXPS-P-F. (D) *Ex situ* Mn L-edge sXAS spectra of DRXPS-P-F.

V-charged and 3.5-V discharged states have similar Mn K-edge spectra, whereas the 2.5 V-discharged and 1.5 V-discharged states have similar spectra that differ from the former three. With further comparisons to the reference spectra of MnO (Mn²⁺), Mn₂O₃ (Mn³⁺), and MnO₂ (Mn⁴⁺) (dash lines in Figure 5C), we conclude that Mn has predominantly +4 valence in the pristine, 4.8 V-charged, and 3.5 V-discharged states, and +3 valence in the 2.5 V-discharged and 1.5 V-discharged states. The big shift in the peak position from 3.5 to 2.5 V suggests that Mn³⁺/Mn⁴⁺ redox should be the main contributor to capacity below 3.5 V versus Li/Li⁺. Note that capacity in charge from 3.0 to ~4.4 V should come from Mn³⁺/Mn⁴⁺, suggested by the close resemblance of the charge curve to that of spinel LiMn₂O₄ with only Mn³⁺/Mn⁴⁺ redox [15, 27]. This could be contributed by the residual Mn3+ formed during synthesis. Above ~4.4 V, oxygen should be the main contributor to capacity since the Mn K-edge barely shifts between pristine and 4.8 V-charged states, and the charge curve from ~4.4 to 4.8 V resembles that of Li-rich layered cathodes or DRX cathodes, which typically features oxygen redox in this voltage range [6, 28-30]. Consistent conclusions can also be drawn from the sXAS measurement on the Mn L-edge (Figure 5D), which shows that the pristine, 4.8 V-charged, and 3.5 V-discharged states have peaks close to that of Mn⁴⁺, while the 2.5 V-discharged and 1.5 V-discharged states have peaks close to that of Mn3+. We may also conclude that minute Mn²⁺ even forms when discharged to 1.5 V. The proposed redox mechanism is indicated by the color scheme shown under the voltage profile in Figure 5A. Notably, the mechanism can stand after extended cycles, as evidenced by HR-XPS, which shows Mn in the +4 oxidation state at the charged state after more than 200 cycles (Supporting Information S1: Figure S7A). To further resolve subtle changes in Mn oxidation state and disentangle overlapping redox processes, future studies with higher-resolution XANES scans and complementary techniques such as resonant inelastic X-ray scattering (RIXS) will be essential.

In addition, even assuming a full Mn³⁺/Mn⁴⁺ conversion for all Mn in DRXPS-P-F, it would only account for 196 mAh g⁻¹ capacity according to the stoichiometry, which is less than the 266 mAh g⁻¹ discharge capacity that was measured experimentally for the first cycle, and even the 200 mAh g⁻¹ discharge capacity for up to the 180th cycle. Meanwhile, a full Mn³⁺/Mn⁴⁺ conversion in DRX-Nb-F would account for 176 mAh g⁻¹, which surpasses its discharge capacity at the 20th cycle. Thus, we conclude that oxygen redox can sustain roughly up to 180 cycles for DRXPS-P-F, and only to ~20 cycles for DRX-Nb-F (Supporting Information S1: Figure S10). From dQ/dV analysis, we observe a high-voltage feature above ~4.1 V versus Li/Li⁺ for DRXPS-P-F that persists over extended cycling (Supporting

6 Interdisciplinary Materials, 2025

Information S1: Figure S11A), which can be attributed to oxygen redox [31, 32], whereas the capacity in this region for DRX-Nb-F quickly vanishes (Supporting Information S1: Figure S11B). These further justify effective oxygen stabilization by phosphorus addition.

3 | Conclusions

We have reported a new DRXPS composition with PO₄ polyanions and F⁻ addition. We demonstrated that P⁵⁺ can be a superior cationic charge compensator to the commonly used Nb⁵⁺ in rocksalt-type cathodes. First, P⁵⁺ can facilitate spineltype cation ordering that offers improved Li⁺ diffusion kinetics than the disordered rocksalt structure favored by Nb5+ addition. Second, better cycling stability is achieved by the P⁵⁺-containing composition over the Nb⁵⁺ counterpart due to strong P-O covalent bonds that enhance structural stability. This work strongly supports the promise of DRXPS as nextgeneration sustainable battery cathodes and the immense potential for further exploration. It validates the design concept of DRXPS cathodes that polyanions can effectively stabilize labile oxygen, and expands the compositional space of DRXPS cathodes to include F⁻, a powerful anionic charge compensator for DRX cathodes.

4 | Experimental

4.1 | Materials Synthesis

DRXPS-P-F and DRX-Nb-F were synthesized using a one-pot low-temperature mechanochemical synthesis method. Stoichiometric amounts of Li₂O (Alfa Aesar, 99.5% purity), MnO₂ (Sigma-Aldrich, 99% purity), LiF (Sigma-Aldrich, 99% purity), Nb₂O₅ (Alfa Aesar, 98.5% purity), and Li₃PO₄ (Sigma-Aldrich, 99% purity) were mixed using the Fritsch Pulverisette 7 Premium Line ball mill. The precursor powders with a total weight of around 5 g were put into an 80 mL stainless-steel jar, with 25 10-mm-diameter stainless-steel balls (weight ratio of powder to ball was 1:20), and mixed in air under 800 rpm for 5 h. No external heat treatment was involved during synthesis.

4.2 | Characterizations

Inductively coupled plasma optical emission spectrometry (ICPOES) was conducted on Agilent 730 for lithium, manganese, niobium, and phosphorus. X-ray diffraction (XRD) was conducted on a PANalytical X'Pert PRO X-ray diffractometer using a Cu target under 45 kV and 40 mA, in the 2θ range of 10–85°. Rietveld refinement was performed using GSAS II [33]. *Ex situ* Raman spectroscopy was conducted on WITec alpha300 R Raman microscope to characterize the local structures of DRXPS-P-F at different states of charge. Laser wavelength of 785 nm was applied with a power of 5 mW, a grating of 300 g mm⁻¹, and a spectral resolution of 0.1 cm⁻¹ to acquire all Raman data. Each spectrum was collected with 5 scans and 10 s integration for each scan. SEM and energy-dispersive spectroscopy (EDS) were conducted on a Zeiss Merlin high-resolution SEM. High-resolution transmission electron microscopy (HRTEM) and selected area

electron diffraction (SAED) were conducted on a JEOL 2010F transmission electron microscope with an acceleration voltage of 200 kV. X-ray fluorescence (XRF) was performed on a Bruker Tracer-III SD Portable XRF. Thermogravimetric analysis (TGA) was conducted on TA Instruments TGA 5500. High-resolution X-ray photoelectron spectroscopy (HR-XPS) was conducted on the Thermo Scientific K-Alpha+ XPS System with a monochromated Al K_{\alpha} source. Survey scans were recorded using the 400 µm spot size mode with a pass energy of 200 eV. C 1s, O 1s, Li 1s, Mn 2p, and P 2p elemental scans were acquired with a pass energy of 50 eV. Binding energies are referenced to the adventitious C 1s peak at 284.8 eV. Peak fittings for Mn 2p and P 2p spectra were performed in CasaXPS using Gaussian (70%)-Lorentzian (30%) profiles for each component. Ex situ soft X-ray absorption spectroscopy (sXAS) measurements were conducted at the IOS (23-ID-2) beamline at the National Synchrotron Light Source II, Brookhaven National Laboratory. Spectra were acquired in partial fluorescence yield (PFY) mode using an energy-discriminating Vortex EM silicon drift detector. Ex situ X-ray absorption near-edge structure (XANES) mapping was conducted at the FXI (18-ID) beamline at the National Synchrotron Light Source II, Brookhaven National Laboratory. All ex situ electrode samples (for Raman, XRD, XPS, sXAS and XANES) were prepared by disassembling coin cells charged/ discharged to a specific voltage, and rinsing with dimethyl ether for 2 min.

4.3 | Electrochemical Testing

Electrodes for electrochemical testing were prepared by mixing 70 wt% active materials (DRXPS-P-F or DRX-Nb-F), 20 wt% conductive carbon (Timcal Super C65), and 10 wt% polyvinylidene fluoride (PVDF, Sigma Aldrich) using N-methyl-2-pyrrolidone (NMP, Sigma Aldrich) as the solvent to form a slurry, which was then cast onto an aluminum foil using a 250 µm-gap doctor blade. The loading of the electrode films was 2-3 mg cm⁻². A polypropylene (PP, Celgard 2400) membrane was used as the separator. 1.2 M LiPF₆ dissolved in ethylene carbonate (EC):diethylene carbonate (DEC) = 30:70 wt% solution (Gotion) was used as the electrolyte. Li metal foil was used as the counter and reference electrode. Coin-type cells (CR2032) were assembled in an argon-filled glove box (MBraun). Electrochemical testing of the coin cells was conducted on a Landt CT2001A battery tester (Wuhan Lanhe Electronics) at room temperature. Galvanostatic cycling was performed between 1.5 and 4.8 V versus Li/Li⁺ at a current of 50 mA g⁻¹, following three formation cycles at 20 mA g⁻¹. Rate performance tests were performed between 1.5 and 4.8 V versus Li/Li⁺ at currents of 20, 50, 100, 200, and 1000 mA g⁻¹. Galvanostatic intermittent titration technique (GITT) was performed between 1.5 and 4.8 V versus Li/Li⁺ with a titration current of 20 mA g⁻¹ for 30 min followed by a 3-h relaxation step.

Differential electrochemical mass spectrometry (DEMS) was conducted with a customized Swagelok cell. Components used in the Swagelok cell were the same as in the coin cells for electrochemical testing. The Swagelok cell was purged with an argon flux of 1 mL min $^{-1}$ for 5 h. Then the cell was charged and discharged at $100\,\mathrm{mA\,g^{-1}}$ for two cycles by using a Landt CT2001A battery tester (Wuhan Lanhe Electronics) at room

temperature. The evolved gases were carried into a mass spectrometer by the argon gas that was continuously purged into the cell.

Author Contributions

Y.H., Y.D., and J.L. conceived the project. Y.H. synthesized the materials and conducted XRD, SEM, DEMS, and ICP-OES measurements. Y.H., Y.N., and Z.Z. contributed to electrochemical testing. Z.L. contributed to XPS measurements. W.C. contributed to Raman measurements. W.C. and V.Y.L. contributed to EDS mapping and TEM imaging. I.W. and A.H. contributed to sXAS measurements. X. X. contributed to XANES measurements. Y.H., Y.D. analyzed the data. Y.H., Y.D., and J.L. wrote the paper. All authors discussed and contributed to the writing.

Acknowledgments

Y.D. acknowledges the support sponsored by Tsinghua-Toyota Joint Research Fund. This study used resources of 18-ID and 23-ID-2 of the National Synchrotron Light Source II, a U.S. Department of Energy (DOE) Office of Science User Facility operated for the DOE Office of Science by Brookhaven National Laboratory under Contract No. DE-SC0012704.

Conflicts of Interest

The authors declare no conflicts of interest.

Data Availability Statement

Data supporting this work are available in the manuscript and the ESI.

References

- 1. J. B. Goodenough and K. S. Park, "The Li-ion Rechargeable Battery: A Perspective," *Journal of the American Chemical Society* 135, no. 4 (2013): 1167–1176.
- 2. S. Ahmed, P. A. Nelson, K. G. Gallagher, N. Susarla, and D. W. Dees, "Cost and Energy Demand of Producing Nickel Manganese Cobalt Cathode Material for Lithium-ion Batteries," *Journal of Power Sources* 342 (2017): 733–740.
- 3. J. Lee, A. Urban, X. Li, D. Su, G. Hautier, and G. Ceder, "Unlocking the Potential of Cation-Disordered Oxides for Rechargeable Lithium Batteries," *Science* 343, no. 6170 (2014): 519–522.
- 4. J. Lee, D. A. Kitchaev, D. H. Kwon, et al., "Reversible Mn²⁺/Mn⁴⁺ Double Redox in Lithium-Excess Cathode Materials," *Nature* 556, no. 7700 (2018): 185–190.
- 5. R. J. Clément, Z. Lun, and G. Ceder, "Cation-Disordered Rocksalt Transition Metal Oxides and Oxyfluorides for High Energy Lithium-ion Cathodes," *Energy & Environmental Science* 13, no. 2 (2020): 345–373.
- 6. Z. Lun, B. Ouyang, D. H. Kwon, et al., "Cation-Disordered Rocksalt-Type High-Entropy Cathodes for Li-ion Batteries," *Nature Materials* 20, no. 2 (2021): 214–221.
- 7. H. M. Hau, T. Holstun, E. Lee, et al., "Disordered Rocksalts as High-Energy and Earth-Abundant Li-ion Cathodes," *Advanced Materials* (2025): 2502766, https://doi.org/10.1002/adma.202502766.
- 8. H. Li, R. Fong, M. Woo, et al., "Toward High-Energy Mn-Based Disordered-Rocksalt Li-ion Cathodes," *Joule* 6, no. 1 (2022): 53–91.
- 9. Y. Huang, Y. Dong, Y. Yang, et al., "Integrated Rocksalt-Polyanion Cathodes With Excess Lithium and Stabilized Cycling," *Nature Energy* 9 (2024): 1497–1505.
- 10. J. Lee, J. K. Papp, R. J. Clément, et al., "Mitigating Oxygen Loss to Improve the Cycling Performance of High Capacity Cation-Disordered Cathode Materials," *Nature Communications* 8, no. 1 (2017): 981.

- 11. D. A. Kitchaev, Z. Lun, W. D. Richards, et al., "Design Principles for High Transition Metal Capacity in Disordered Rocksalt Li-ion Cathodes," *Energy & Environmental Science* 11, no. 8 (2018): 2159–2171.
- 12. Z. Lun, B. Ouyang, Z. Cai, et al., "Design Principles for High-Capacity Mn-Based Cation-Disordered Rocksalt Cathodes," *Chem* 6, no. 1 (2020): 153–168.
- 13. B. Ouyang, N. Artrith, Z. Lun, et al., "Effect of Fluorination on Lithium Transport and Short-Range Order in Disordered-Rocksalt-Type Lithium-ion Battery Cathodes," *Advanced Energy Materials* 10, no. 10 (2020): 1903240.
- 14. N. J. Szymanski, Y. Zeng, T. Bennett, et al., "Understanding the Fluorination of Disordered Rocksalt Cathodes Through Rational Exploration of Synthesis Pathways," *Chemistry of Materials* 34, no. 15 (2022): 7015–7028.
- 15. Y. Huang, Y. Dong, S. Li, et al., "Lithium Manganese Spinel Cathodes for Lithium-ion Batteries," *Advanced Energy Materials* 11, no. 2 (2021): 2000997.
- 16. M. M. Thackeray, "Spinel Electrodes for Lithium Batteries," *Journal of the American Ceramic Society* 82, no. 12 (1999): 3347–3354.
- 17. Z. Lun, B. Ouyang, D. A. Kichaev, et al., "Improved Cycling Performance of Li-Excess Cation-Disordered Cathode Materials Upon Fluorine Substitution," *Advanced Energy Materials* 9, no. 2 (2019): 1802959.
- 18. C. M. Julien and M. Massot, "Lattice Vibrations of Materials for Lithium Rechargeable Batteries III. Lithium Manganese Oxides," *Materials Science and Engineering: B* 100, no. 3 (2003): 69–78.
- 19. J. Wu, G. K. P. Dathar, C. Sun, et al., "In Situ Raman Spectroscopy of LiFePO₄: Size and Morphology Dependence During Charge and Self-Discharge," Nanotechnology 24, no. 42 (2013): 424009.
- 20. E. Markevich, R. Sharabi, O. Haik, et al., "Raman Spectroscopy of Carbon-Coated LiCOPO₄ and LiFePO₄ Olivines," *Journal of Power Sources* 196, no. 15 (2011): 6433–6439.
- 21. J. D. Pless, T. J. Garino, J. E. Maslar, and T. M. Nenoff, "Tunable Conductivity of Collapsed Sandia Octahedral Molecular Sieves," *Chemistry of Materials* 19, no. 20 (2007): 4855–4863.
- 22. J. M. Jehng and I. E. Wachs, "Structural Chemistry and Raman Spectra of Niobium Oxides," *Chemistry of Materials* 3, no. 1 (1991): 100–107.
- 23. H. Ji, J. Wu, Z. Cai, et al., "Ultrahigh Power and Energy Density in Partially Ordered Lithium-ion Cathode Materials," *Nature Energy* 5, no. 3 (2020): 213–221.
- 24. M. M. Thackeray, W. I. F. David, P. G. Bruce, and J. B. Goodenough, "Lithium Insertion Into Manganese Spinels," *Materials Research Bulletin* 18, no. 4 (1983): 461–472.
- 25. W. J. Zhang, "Structure and Performance of LiFePO₄ Cathode Materials: A Review," *Journal of Power Sources* 196, no. 6 (2011): 2962–2970.
- 26. M. Yoon, Y. Dong, J. Hwang, et al., "Reactive Boride Infusion Stabilizes Ni-Rich Cathodes for Lithium-ion Batteries," *Nature Energy* 6, no. 4 (2021): 362–371.
- 27. D. K. Kim, P. Muralidharan, H. W. Lee, et al., "Spinel LiMn $_2O_4$ Nanorods as Lithium-ion Battery Cathodes," *Nano Letters* 8, no. 11 (2008): 3948–3952.
- 28. G. Assat and J. M. Tarascon, "Fundamental Understanding and Practical Challenges of Anionic Redox Activity in Li-ion Batteries," *Nature Energy* 3, no. 5 (2018): 373–386.
- 29. J. Hong, W. E. Gent, P. Xiao, et al., "Metal-Oxygen Decoordination Stabilizes Anion Redox in Li-Rich Oxide," *Nature Materials* 18, no. 3 (2019): 256–265.
- 30. Z. Zhu, D. Yu, Y. Yang, et al., "Gradient Li-Rich Oxide Cathode Particles Immunized Against Oxygen Release by a Molten Salt Treatment," *Nature Energy* 4, no. 12 (2019): 1049–1058.

8 Interdisciplinary Materials, 2025

- 31. T. Y. Huang, M. J. Crafton, Y. Yue, W. Tong, and B. D. McCloskey, "Deconvolution of Intermixed Redox Processes in Ni-Based Cation-Disordered Li-Excess Cathodes," *Energy & Environmental Science* 14, no. 3 (2021): 1553–1562.
- 32. T. Y. Huang, Z. Cai, M. J. Crafton, et al., "Quantitative Decoupling of Oxygen-Redox and Manganese-Redox Voltage Hysteresis in a Cation-Disordered Rock Salt Cathode," *Advanced Energy Materials* 13, no. 21 (2023): 2300241.
- 33. B. H. Toby and R. B. Von Dreele, "GSAS-II: The Genesis of a Modern Open-Source All Purpose Crystallography Software Package," *Journal of Applied Crystallography* 46, no. 2 (2013): 544–549.

Supporting Information

Additional supporting information can be found online in the Supporting Information section.